Miniature electron beam separator based on three stacked dipoles

Krielaart, M. A.R.; Maas, D. J.; Loginov, S. V.; Kruit, P.

DOI
10.1063/5.0008089

Publication date
2020

Document Version
Final published version

Published in
Journal of Applied Physics

Journal of Applied Physics

Miniature electron beam separator based on three stacked dipoles

Cite as: J. Appl. Phys. **127**, 234904 (2020); https://doi.org/10.1063/5.0008089
Submitted: 18 March 2020 . Accepted: 30 May 2020 . Published Online: 16 June 2020

M. A. R. Krielaart, D. J. Maas, S. V. Loginov, and P. Kruit

Journal of Applied Physics ARTICLE scitation.org/journal/jap

Miniature electron beam separator based on three stacked dipoles

Cite as: J. Appl. Phys. **127**, 234904 (2020); doi: 10.1063/5.0008089
Submitted: 18 March 2020 · Accepted: 30 May 2020 ·
Published Online: 16 June 2020

View Online Export Citation CrossMark

M. A. R. Krielaart,[1,a)] D. J. Maas,[1,2] S. V. Loginov,[1] and P. Kruit[1]

AFFILIATIONS

[1]Department of Imaging Physics, Faculty of Applied Sciences, Delft University of Technology, Lorentzweg 1, 2628 CJ Delft, The Netherlands
[2]Nano-Instrumentation Department, Netherlands Organization for Applied Scientific Research, TNO, Stieltjesweg 1, 2628CK Delft, The Netherlands

[a)]**Author to whom correspondence should be addressed:** m.a.r.krielaart@tudelft.nl

ABSTRACT

We designed and built a compact bi-axial electron beam separator. This separator is an indispensable electron optical element in the development of MEMS-mirror-based miniaturized concepts for quantum electron microscopy (QEM) and aberration-corrected low-voltage scanning electron microscopy (AC-SEM). The separator provides the essential cycling of the electron beam between the two parallel optical axes that are part of these systems. This requires crossed electric and magnetic fields perpendicular to the beam path, as can be found in Wien-filter type beam separators. In our miniaturized QEM or AC-SEM concepts, the parallel axes are separated by only 1 mm. Conventional Wien-filter-based beam separator concepts rely on in-plane electric and magnetic multipole electrode configurations that are larger than the restricted available volume in these miniaturized QEM/AC-SEM systems. Our compact beam separator design introduces three stacked dipole electrode layers, which enables simultaneous beam separation at two parallel axes that are in close proximity. The outer layer electrodes maintain an electric field for which the direction on the one axis is opposed to that on the other axis. The middle layer generates a perpendicularly oriented magnetic field that spans both axes. The total field configuration enables the deflection of the beam on one axis and simultaneously provides a straight passage on the other axis. The deflection strength and distortion fields of the beam separator are experimentally obtained with a 2 keV electron beam energy. The results validate the use of the beam separator for electron energies up to 5 keV and deflection angles up to 100 mrad.

I. INTRODUCTION

Advanced inspection and analysis equipment such as electron microscopes, mass spectrometers, and focused ion beam systems contain sophisticated optical elements. These elements control the charged particles both in the primary beam and in the secondary electron or ion signals. In most of these instruments, a beam separator is an important element in which the primary beam and the secondary beams are separated with a negligible impact on both the qualities of the primary beam and the secondary beam strength,[1] thus enabling efficient high quality imaging and analysis.

Charged particle beams can be manipulated with electric and magnetic fields through the Lorentz force. While propagating through a dipole field, a charged particle beam is accelerated and/or deflected. In the special case of a spread out beam that traverses a cleverly arranged series of multipole fields, aberration correction is also achieved.[2] As the Lorentz force is dependent on both beam energy and direction, crossed electric (E) and magnetic (B) dipole fields provide zero deflection for exactly one beam energy only, for which the Wien condition $E = vB$ is satisfied. Consequently, a polychromatic beam that propagates a crossed E and B field is dispersed. The amount of dispersion is controlled by the magnitude of the fields. Beam energy analyzers such as a Wien filter[3] make use of the latter effect to measure the energy spectrum of a beam[4] and to restore longitudinal coherence in interferometers.[5] When a Wien filter is combined with a narrow aperture slit positioned behind the exit port, a monochromator is realized.[6,7] Furthermore, overlapping perpendicular electric and magnetic fields find application in beam separators, for which the deflection angle upon propagation depends on the sign of the velocity vector.

When combining a beam separator with a beam-reflecting element, for instance, an aperture mirror as in (aberration-corrected) low-energy electron microscopy[8] and/or a specimen at cathode potential as seen in a low energy/photoemission electron microscope (LEEM/PEEM)[9–11] and mirror electron microscopy,[12] again the need arises to separate the trajectories of the incident and reflected particles. For these cases, there are even more challenging constraints on, e.g., the separator size and its optical properties,[1] since the uncorrectable aberrations cannot easily be de-magnified to have a negligible impact on the (improved) primary beam probe size.

In particular, for recent suggestions for aberration correction[8] and beam patterning,[13] both setups (Fig. 1) are enabled by the use of sub-mm-sized accurate electrodes that are manufactured using MEMS production technology.[14] As a consequence of the miniaturization, the lateral separation between the microscope axis and the mirror axis is only 1 or 2 mm, leaving a too restricted space for both conventional and state of the art miniature[15,16] beam separators.

In this paper, we present the design, construction, and evaluation of a compact electron optical beam separator that facilitates most of the above-mentioned configurations. In our novel beam separator design, crossed *E*- and *B*-dipole fields are applied after each other, rather than at the same axial position as in conventional Wien-filter designs. Our prototype consists of three layers of perpendicularly arranged dipoles. Similar to what is seen in Mook's monochromator,[6] the magnetic poles can also be used as electrostatic poles, which has the practical benefit of well-matching fringe fields. The beam is deflected in one plane by passing a sequence of E–B–E dipole fields, and in the perpendicular plane by a sequence of B–E–B dipole fields. We coin the term EBE separator for this device.

Because of the initial application of the beam separator in low-voltage scanning electron microscopy (SEM) and for miniature setups as we described above, the design that we present here is aimed at single digit keV beam energies, and deflection angles up to 100 mrad. The axes are laterally separated by 1 mm. We will obtain multipole distortion coefficients that enable to determine the limit of the beam spread in the device that is tolerable in the case of integration with setups in which the crossover plane of the beam does not coincide with the device, such as shown in Fig. 1(b).

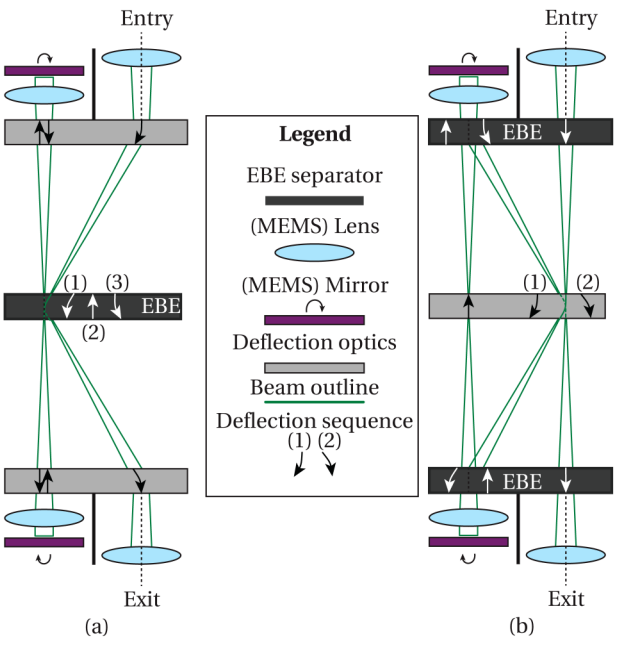

FIG. 1. MEMS based multi-axis electron optical setups, based on proposals for (a) miniaturized double electron mirror based aberration correction for scanning electron microscopy and (b) mirror based beam patterning. The beam enters from the top on the right hand side axis and propagates through the setup as indicated by the beam outline (green) and deflection sequence (numbered arrow). The use of MEMS electron optics enables small deflection angles (below 100 mrad), such as to limit deflection dispersion errors. The EBE separator units indicate optical planes that require a directional dependent deflection. Other deflection optics relies on electrostatic deflection fields only.

II. EBE ELECTRON OPTICS

A. Beam separator

The function of a beam separator is to provide either a deflection trajectory or straight path for the incident beam,[1] depending on the sign of the velocity vector. Simple beam separators exhibit (shared) in-plane magnetic and electric fields and require a single electric and a single magnetic field that are rotated 90° in-plane with respect to each other in order to facilitate both trajectories. Consequently, the electrode geometry will not only result in a dipole (deflection) field but also a higher order hexapole field is generated.

For this reason, we separate the electric and magnetic fields spatially behind one another. This enables the use of flat dipole electrodes. However, the use of only two dipole layers would not suffice as the net effect for the supposed straight path would result in a beam shift as the dipole fields do not overlap in space [Fig. 2(a)]. Hence, it is required to add a third dipole layer and distribute either the electric or magnetic field contribution equally over the top and bottom layers [Fig. 2(b)]. This way, the straight path through the beam separator will not suffer from a beam shift, while the deflection trajectory angle can still be set independently.

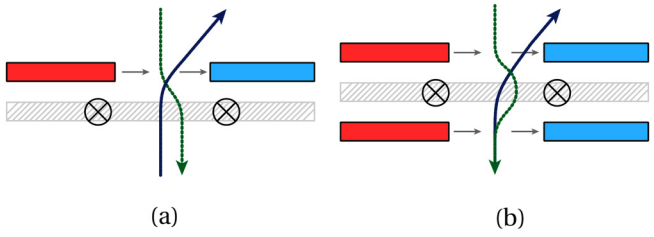

FIG. 2. (a) The schematic beam path through two consecutive dipole fields (one electric, one magnetic) and (b) the schematic beam path through three consecutive dipole fields (two electric, one magnetic). The electric field is distributed equally among the top and bottom layers and balances the deflection through the middle magnetic field. Notice that the role of magnetic and electric fields can be interchanged.

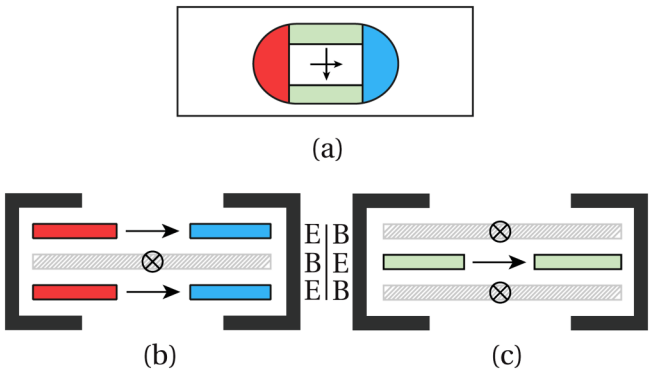

FIG. 3. Schematic representation of the electrodes and field orientation inside the beam separator. (a) Top view, with the elongated entrance slit (gray), primary electric (red and blue), and magnetic (green) poles visible. (b) Horizontal cross section view of the beam separator, with the in-plane electric field and out-of-plane magnetic field arrows. (c) Vertical cross section view, perpendicular to the view of (b), showing the direction of the generated fields. The signs of the fields are all interchangeable.

Two configurations of fields comply with the above:

1. E–B–E: the electric dipole is equally distributed among the first and third level dipole and the magnetic field is generated on the second layer [Fig. 3(b)].
2. B–E–B: the magnetic field is equally distributed among the first and third level dipole and the electric field is generated on the second layer [Fig. 3(c)].

Both configurations can be set independently of each other, and the two resulting deflection planes are perpendicular to one another.

The first order effect of an excitation in one of the dipole layers can be obtained by calculating the velocity change in the direction of the resulting force upon traversing the field. For an electric dipole, the deflection angle (α_E) is dependent on the beam energy Φ (in V) and the strength of the electric field (E_x) as well as the effective length ℓ_{eff}, via

$$\alpha_E = \frac{E_x \ell_{\text{eff}}}{2\Phi}. \tag{1}$$

The effective length relates to the thickness ℓ of the electrode that generates the field through the constant $k \equiv \ell_{\text{eff}}/\ell$ and accounts for the fringe fields in the first order top hat model. A value for the effective length can be obtained either through numerical modeling or matching of the deflection term to experimental data. For a magnetic induction field (B_y) dipole, the deflection angle is by

$$\alpha_B = \sqrt{\frac{e}{m}} \frac{B_y \ell_{\text{eff}}}{\sqrt{2\Phi}}. \tag{2}$$

In both equations, a top hat field is assumed in order to account for the fringe fields. The net deflection angle α that the beam obtains upon passage through the device is given by the sum of the contribution from each of the three layers.

From a numerical COMSOL model, the on-axis magnetic and electric field strength is obtained for the E–B–E configuration (in-plane deflection) as well as the B–E–B configuration (out-of-plane deflection) (Fig. 4). In the model, an excitation current of 1 A and an electric potential of ± 1 V across the optical axis are used. From these data, the effective length is determined by equating the integrated on-axis fields to the top hat model, given by

$$\int F(z)\, dz = F_0 \ell_{\text{eff}}. \tag{3}$$

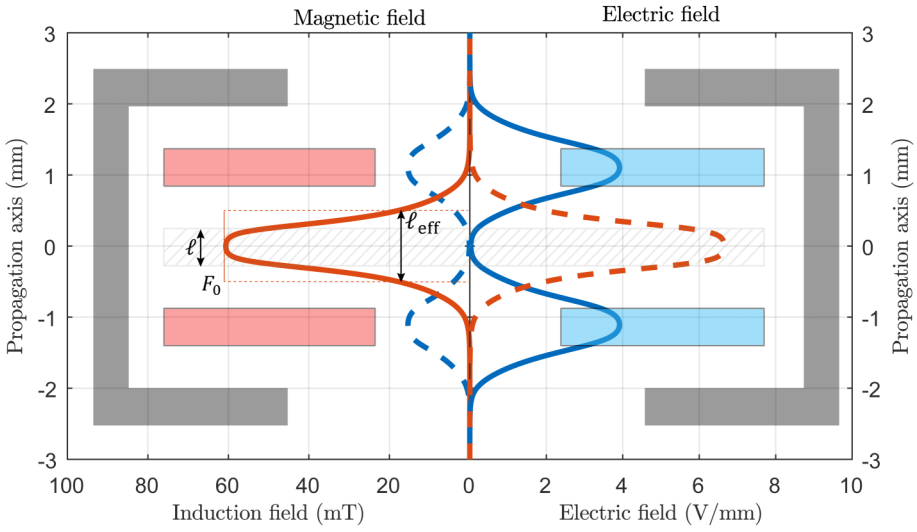

FIG. 4. Axial (left) magnetic induction and (right) electric field strength components for fields that provide a net force on the beam in the in-plane (solid) and out-of-plane (dashed) direction. An excitation current of 1 A and a potential of ± 1 V were used for this calculation. The definitions for the electrode thickness (ℓ) and effective field length (ℓ_{eff}) are indicated for the middle layer.

Here, $F(z)$ represents the numerical solution data for the electric or magnetic field and F_0 is the nominal field strength that is used in the top hat model. Application of Eq. (3) on the numerical data yields a value of $k_{t+b} = 1.88$ for a combined excitation of the field at the top and bottom layers and $k_m = 1.75$ for a field excitation at the middle layer.

B. Beam separator for two parallel axes

We discussed in the introduction two microscope schemes (Fig. 1) that would benefit from the presence of a second axis. This axis should run in parallel and be separated with the optical axis over a lateral distance of the order of magnitude 1 mm. The concept of the beam separator with one optical axis can be extended to include this second axis that is placed in parallel with the first axis. The resulting E–B–E and B–E–B field configurations (Fig. 5) then explicitly take into account the presence of the entry or exit trajectories for MEMS based setups that contain reflective elements.

The geometry of the beam separator for two parallel axes differs from the single-axis design only in the top and bottom dipole layers. In these layers, an anti-parallel electric or magnetic field is added with respect to the single-axis design, whereas the geometry of the middle layer is unchanged from the single-axis design. Hence, the effect of the middle layer field is the same for both axes, whereas the effect of the top and lower layers is opposite for both axes.

For this two-axes design, the E–B–E field configuration will deflect the beam in the direction of the parallel axis and thus realize the electron trajectories as shown earlier (Fig. 1). Simultaneously, the B–E–B field configuration enables the deflection of the beam perpendicular to the plane that is spanned by the two axes. The latter offers a practical means of correcting for small (mechanical) alignment errors.

C. Energy filter

The dispersion relationships for the electric and magnetic fields are derived by obtaining the derivative of the deflection angle formulas with respect to the beam energy. This yields two simple equations that relate the deviation in deflection angle ($\Delta\alpha$) as a function of the deviation of the beam energy ($\Delta\Phi$) from the nominal energy (Φ), given by

$$\Delta\alpha_E = \frac{\Delta\Phi}{\Phi}\alpha \tag{4}$$

and

$$\Delta\alpha_B = \frac{1}{2}\frac{\Delta\Phi}{\Phi}\alpha \tag{5}$$

for, respectively, the electric and magnetic deflection dispersion. Ordinary energy filters rely on the factor two difference between the magnetic and electric dispersion relation since the fields that provide the net zero deflection, $\alpha_E = -\alpha_B$ overlap,

$$\frac{\Delta\Phi}{\Phi} = \frac{\Delta\alpha_E}{\alpha_E} = 2\frac{\Delta\alpha_B}{\alpha_B}. \tag{6}$$

In our device, the three dipole fields are separated in space, which does not change the outcome of the above analysis to first order.

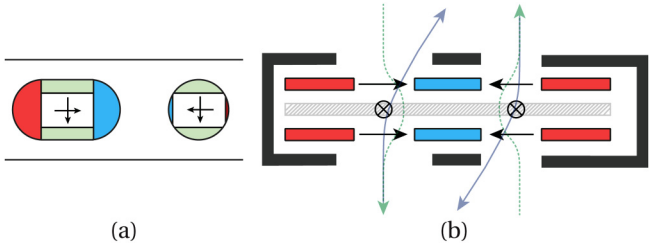

FIG. 5. Schematic representation of the electrodes and field orientation inside the beam separator for two parallel axes. (a) Top view showing the entrance apertures (gray) and inside electrodes. (b) Direction of the fields inside the device, with respect to the various electrodes. The field in the top and bottom layers always points in the opposite direction for both axes. The central field is shared across both axes and thus performs an axis-independent action on the beam. Resulting beam trajectories for electrode excitations that satisfy the Wien condition are shown. The perpendicular cross section is unchanged from the single-axis design and not shown here again.

D. Higher order effects

Our main motivation for splitting the electric and magnetic deflection layers results from the attempt of reducing the generation of higher order distortion fields. By choosing the sideways extend of the electrodes much larger than the longitudinal spacing between the dipole electrodes, we aim to eliminate the higher harmonic field distortions that are associated with more complex shaped electrodes.

The geometry that we described for the beam separator with either one axis or two axes allows for the generation of dipole fields. In the presence of a single dipole layer, no higher order distortion can develop, neither in between the electrodes nor as a result of the fringe fields at the edge of the electrode pair.

However, the addition of multiple crossed layers of dipole electrodes may cause a three-dimensional influence, such that the fringe fields of the separate electrode pairs become deformed under the presence of the neighboring electrode pair. Due to the symmetry of the stacked electrode geometry and due to the asymmetry of the electric and magnetic excitations of the electrode pairs per layer, no quadrupole distortion can be generated. Instead, the first harmonic distortion field that is associated with the device geometry and field configuration is a hexapole.

The deflection and distortion field strength are described quantitatively by a projected potential along the optical axis. This is obtained as the solution of the Laplace equation for non-rotationally symmetric fields[17] with excitation amplitude U_0, given by

$$U(r, \phi) = -U_0 \sum_{n=1}^{N} c_n n r^{n-1} \cos(2\pi n[\phi + \theta_n]). \tag{7}$$

The magnitude (c_n) and orientation angle (θ_n) correspond to the optical dipole field ($n = 1$), astigmatism or quadrupole field

($n = 2$), and higher order fields. Since the deflection angle $\alpha \propto U$ is proportional to the above expression for the potential, the effect of beam propagation through the above field results in a spatial position dependent beam deflection. It must be observed that, except for the dipole field itself, all higher harmonic fields contain an off-axis radial dependence.

Consequently, the first higher order field causes astigmatism to a spread out beam due to the quadrupole field which degrades the size of the (virtual) probe size and the second higher harmonic causes a hexapole distortion in the (virtual) probe. The resulting blur is then obtained by calculating the additional beam deflection α_n for each order and tracing the distinct contributions back to the last image plane at distance u away from the EBE separator. For a beam of radius R_0 inside the separator, the contribution to the probe size degradation is then given by

$$d_n^{\text{spot}} = u c_n n U_0 R_0^{n-1}. \tag{8}$$

It depends on the final application what degree of blurring is tolerated. For the special case where the crossover of the beam coincides with the EBE separator [for instance, in Fig. 1(a)], the effects of higher orders can usually be neglected.

III. ELECTROMECHANICAL DESIGN

In this section, we discuss the construction of the beam separator for two parallel axes. The two-axes implementation covers the functionality that is required for both one- and two-axes beam separation, as well as the other applications that we discussed before. We will discuss the outline, placement, and machining of the electrode poles and device enclosure, the mechanical requirements on alignment, and the integration of the electrical signals into the device.

A. Machining tolerances

The tolerances on machining accuracy and mechanical alignment of the electrodes are dictated by the application of the device. As the device is built up from different layers of dipole geometry, any longitudinal stacking error will affect both axis equally and is of limited concern. In contrast, it is expected machining tolerances will result in variations of dipole gap spacing within the individual layers.

For both magnetic and electric dipole fields, the resulting deflection angle $\alpha \propto w_{\text{gap}}^{-1}$ is inversely proportional to the separation gap width (w_{gap}) of the dipole [Fig. 6(a)]. Hence, a width variation $dw = w_2 - w_1$ between the dipole pair on the one and on the other axis will introduce a deflection angle error ($d\alpha$) that is approximated by

$$d\alpha = -\frac{\alpha}{w_{\text{gap}}}\, dw. \tag{9}$$

In turn, for the mentioned deflection angles for use as a beam separator of up to 100 mrad, the electron trajectory through the effective straight path gets erroneously deflected by approximately 0.1 mrad/μm gap width variation. The above result is mainly

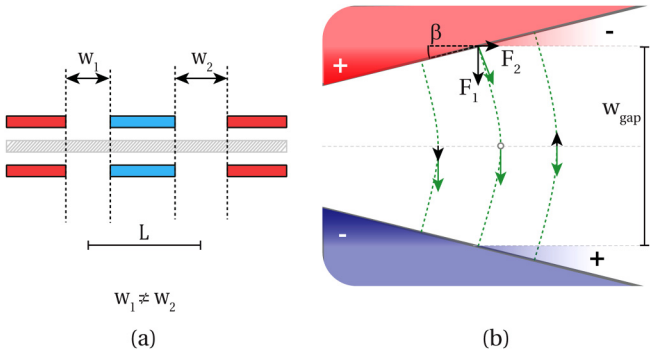

FIG. 6. (a) Gap width mismatch as seen from the side between both axes results in a net deflection error that is proportional to the deflection angle and variation in the gap width. (b) A wedge geometry as seen from above leads to a quadrupole contribution to the deflection field that would ordinarily be absent when $\beta \to 0$.

applicable to the top and bottom layers of the device, as the dipole fields on these layers are not shared across both axes.

A rotation misalignment of a dipole electrode pair leads to multiple optical distortions. The dipole field at the central layer of the device is shared by both axes. Hence, an in-plane rotational placement error between the two electrodes leads to the wedged geometry when seen from the top. The gap width variation $dw_{\text{gap}} = L \tan(\beta)$ then provides the variation in deflection strength across both axes for a given wedge angle (β).

Additionally, the wedge angle leads to a symmetric non-uniformity in the dipole field. This is understood by comparing the dipole field strength, leading to a force F_1 on the beam for a parallel plate geometry ($\beta = 0$), to the additional force F_2 that develops for an increasing wedge angle [see Fig. 6(b)]. The wedge angle β can then be obtained by comparing the (experimentally obtained) dipole (c_1) and quadrupole (c_2) coefficients, which are related through

$$\beta = \tan\left(\frac{c_2}{c_1} w_{\text{gap}}\right). \tag{10}$$

A method for obtaining these coefficients in an experiment is discussed in Sec. IV of this work.

B. Electrodes and enclosure

All electrodes are fabricated from metal that exhibits high magnetic permeability. We used μ-metal to this end, an alloy consistent of 77% Ni, 16% Fe and traces of Cu and Cr. The combination of high magnetic relative permeability of up to 3×10^5 and limited susceptibility to oxidization of the NiFe makes that magnetic and electric fields can be injected away from the optical axis of the device. In addition, μ-metal is known for its limited sensitivity to magnetic hysteresis.[18]

Mechanical stress is known to deteriorate the magnetic properties of μ-metal. For this reason, all electrodes are manufactured

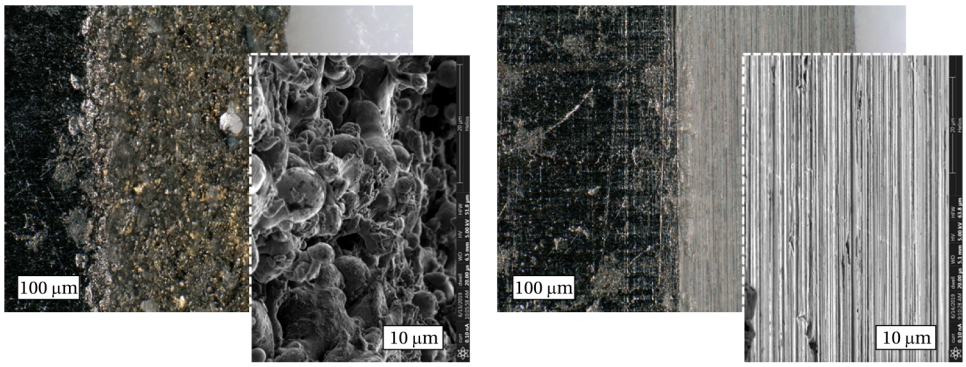

FIG. 7. Optical and SEM inspection photograph and micrograph (tilted) of a spark eroded electrode pole before (left) and after (right) polishing with a fine grain abrasive paper. Notice the yellowish colored sediment in the photograph of the unpolished electrode, which suggests that the spark wire deposits material onto the electrode. No traces of this deposited material were found after the surface treatment.

through the use of spark erosion. The absolute machining accuracy for this technique is limited to approximately 10 μm and thus by following the earlier reasoning, we may expect deflection errors up to 0.1 mrad. During manufacturing, we also noticed that the spark wire deposits the material onto the electrode surface, which causes surface roughness of up to 30 μm that is afterward reduced to bulk roughness by a surface polish (Fig. 7).

The mechanical enclosure of the device is milled out of aluminum alloy Al 7075-T6 (AlZnMgCu1,5). Tangent surfaces are milled into the enclosure to enable the mechanical alignment of the electrodes [Figs. 8(a) and 8(b)]. After milling, the enclosure is dimensionally stable anodized in order to provide electrical insulation of the enclosure toward the electrodes.

The demonstration of principle experiments that we carried out for this work was performed inside an SEM at a beam energy of 2 keV. Because of possible application areas of the EBE beam separator that we showed before (Fig. 1), the two axes in the manufactured device are separated by 1 mm and a deflection angle of approximately 50 mrad must be realized during operation. In the design, care must be taken that the deflected beam path does not collide with the entrance or exit apertures of the device. The use of 0.5 mm thick electrode material and a comparable spacing between the layers results in sufficient clearance between the beam path and the apertures.

C. Electromechanical integration

The electric potentials and the magnetic fluxes are injected into the device through flexible printed circuit boards (fPCBs) [Fig. 8(c)] that are positioned in between the various dipole layers. A total of four identical fPCBs is used for this. The fPCBs each contain four electrical contact pads that are exposed on one side of the fPCBs. The contact pads are rotationally separated by an angle of 90°.

Around each contact pad, a multi-layer coil is integrated in the fPCBs, which is electrically independent of the included contact pad. Each mu-metal electrode is sandwiched in between two of these coils. Consequently, an opposite direction of current through the coil pair that is formed this way allows to either source or sink magnetic flux from the in-between sandwiched mu-metal electrode.

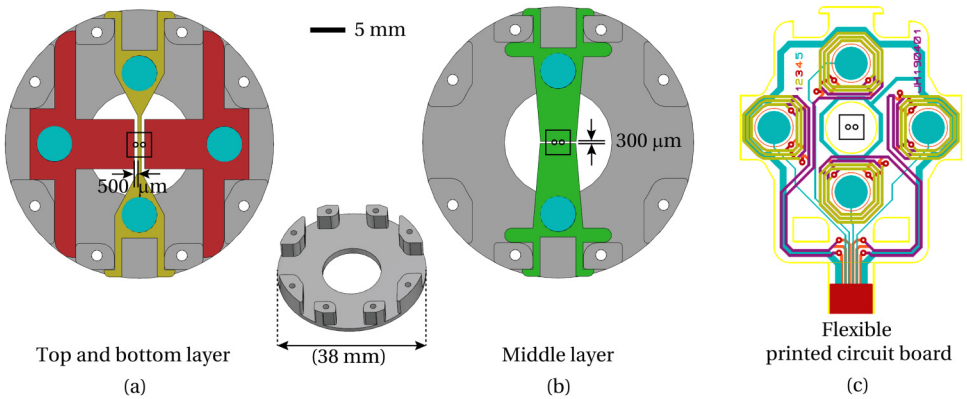

FIG. 8. Mechanical outline of the device enclosure (inset for perspective view) and shape and orientation for (a) the top and bottom layer electrodes and (b) the central layer electrodes. All electrodes are manufactured by spark erosion from mu-metal. The alignment of the elements relies on the tangent surfaces and grips at the circumference of the device enclosure. Electrical contact and magnetic flux injection are achieved through (c) the flexible printed circuit boards (fPCBs). The turquoise islands provide electrical contact for the electrodes and these are surrounded by 12 turn coils (distributed over four layers, three turns per layer). The circles inside the black square indicate the position of both optical axes.

This way, the magnetic dipole fields at the optical axis are generated independently for the top and bottom layers, or the middle layer. The magnetic field lines are closed through the lid of the EBE separator.

Because of the thickness that the multi-layer coils add to the fPCBs, a μ-metal disk is inserted in each of the coils and acts as a magnetic bore. The inserted disk performs a dual role by also providing the electrical interface between the embedded contact pad from the one side and the metal electrode on the other side. The reliability of the electrical contact of the disk toward the electrode may be further improved by gold plating of the disk, although our current results were obtained without performing this step and no indications of poor electrical contact were observed.

IV. EXPERIMENTAL METHODS

We have manufactured and assembled the two-axis beam separator (Fig. 9) and assess the performance through beam deflection measurements. These measurements are performed by positioning the EBE separator on an xy-translation stage inside the specimen chamber of a scanning electron microscope. A series of micrographs is obtained of a specimen that is positioned behind the separator, at increasing excitation field strength and at a beam energy of 2 keV. The resulting deflection strength and higher order multipole coefficients are obtained through numerical analysis of the micrographs.

A. Experimental setup

The experiments are performed inside the specimen chamber of a FEI Verios 640 scanning electron microscope (SEM) by mounting the device onto a custom stage. The mounting structure consists of two vertically separated levels such that the device can be positioned at a fixed distance above the sample plane. By means of two piezo actuators (Physik Instrumente, PI Q-545), we can translate the mounting structure in a plane perpendicular to the optical axis of the microscope for alignment purposes (Fig. 10).

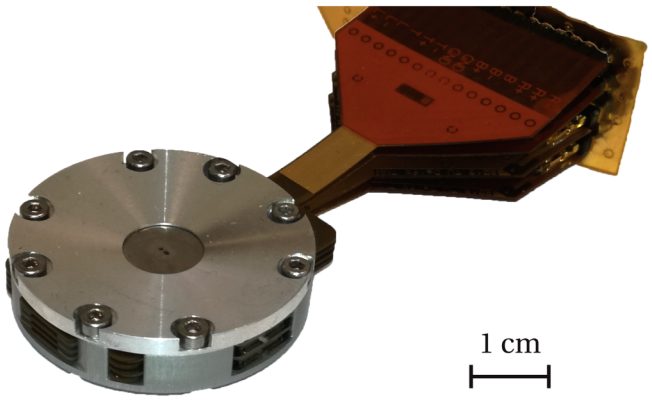

FIG. 9. Photograph of the assembled EBE separator that was used during the experiments. The outer diameter of the holder measures 38 mm and the total thickness of the device (including the cover) measures 9.4 mm.

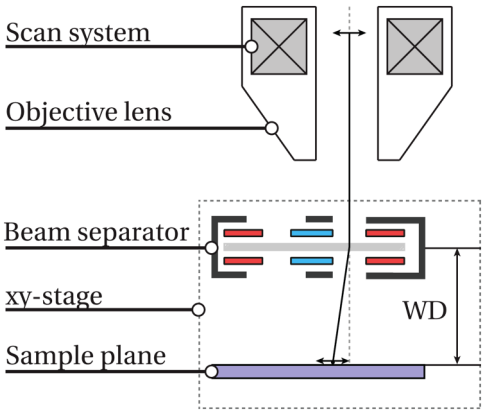

FIG. 10. Schematic of the experimental setup. The beam separator and specimen are placed together on an xy-translation stage inside the specimen chamber of the microscope. The scan system of the microscope provides the scanning and detector logic, and the beam is focused onto the specimen by the normal-mode objective lens of the microscope.

The voltage and current supplies that are used for excitation of the deflection fields are designed and built in-house. The voltage supplies are bipolar with an output range of ± 300 V and are built around a PA91 Apex Microtechnology amplifier chip. The current supply has an output current of ± 500 mA and is centered around a Texas Instruments LM675T amplifier. We make use of a LabVIEW application to control the DT9854 digital-analog converters that are used to program the amplifier output signals. Micrographs are recorded by collecting secondary electrons with the Everhart-Thornley Detector (ETD) positioned inside the SEM chamber.

B. Deflection and distortion fields

Series of micrographs are obtained by scanning the electron beam with the microscope scanning system through one of the axes of the device, while focusing the beam onto a specimen that is positioned behind the separator. The field excitation of the EBE separator is stepwise increased in between the acquisition of each micrograph, which results in a change of beam angle (Fig. 10). After the acquisition, image registration is performed on consecutively recorded micrographs and in this way, we obtain displacement maps that relate corresponding regions in both micrographs. The image registration is performed numerically through an implementation of Speeded Up Robust Features (SURF) based feature recognition[19] in MATLAB.[20] We found that the unpolished side of a single side polished (SSP) Si wafer provides us with sufficient and detailed unique features for the SURF method to work.

From the proportionality [see Eq. (7)] between the projected electric field $U(r, \phi)$ and the distortion field coefficients c_n, the spatial displacement map $\vec{v}(r, \phi)$ of a narrow beam that passes through this field upon small changes (ΔU) in excitation of the

field is given by

$$\vec{v}(r,\phi) = -W\Delta U \sum_{n=1}^{N} c_n n r^{n-1} \cos(2\pi n[\phi + \theta_n]). \quad (11)$$

W is the work distance between the EBE separator and the image plane. The coefficients are extracted from the displacement maps by placement of an analysis circle that is centered on the optical axis [Fig. 11(a)]. The dot product of the tangential vectors that describe the circle ($\vec{\kappa}$) and local displacement vector ($\vec{v}$) offer a quantitative scalar description of local distortion $f(\phi)$, where ϕ is the angle with the positive horizontal axis [Fig. 11(b)]. Analysis of the spectrum of $f(\phi)$ by means of a Fourier transform yields the complex valued coefficients F_n at the circle radius R. These coefficients are related to the multipole coefficients of Eq. (11) through

$$c_n = \frac{|F_n|}{nWR^{n-1}}. \quad (12)$$

The field orientation angle is obtained from the angle of the complex valued coefficient F_n. For $n > 1$, phase wrapping occurs at field orientation angles of $2\pi/n$, which is accounted for in the numerical implementation of the method.

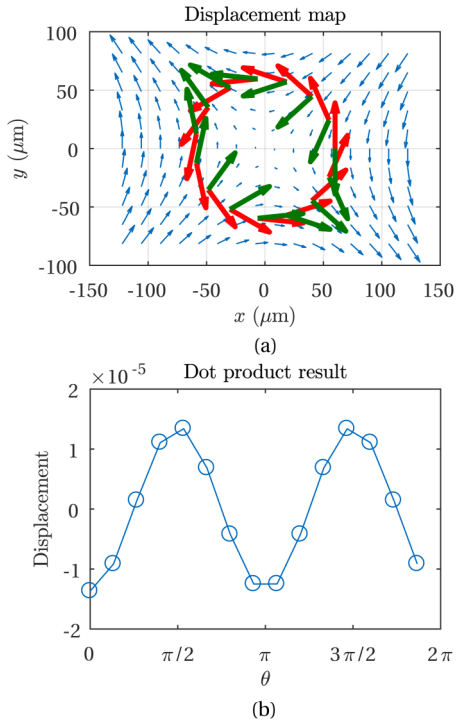

FIG. 11. Outline of the detection method. (a) The displacement map data are interpolated onto a regular spaced grid and the displacement map vectors are shown (blue arrows). The dot product is calculated for the analysis circle tangent vectors $\vec{\kappa}$ (red arrow) and interpolated displacement vectors $\vec{v}$ (green arrows). (b) Result of the dot product calculation for the displacement map shown; a sparse dataset shown for clarity.

C. Detection limit and errors

The deflection caused by order n is dependent on the radial distance from the optical axis, as given by Eq. (1). Hence, the minimum detectable field magnitude varies for each multipole order as the effect only shows up in the displacement map when the effect is at least equal to the distance that corresponds to (a multiple of) one pixel in the recorded micrographs. Hence, weak distortion coefficients can only be discerned from the data when both a large field of view and a small pixel and probe size are used.

In the results that we obtained, the Fourier analysis is performed on a circle radius of 100 μm and this radius is limited by the field of view of the micrograph. The micrographs are recorded at a resolution of 162.8 nm per pixel. Evaluation of Eq. (12) then directly provides the detection threshold for the various distortion coefficients, for a given excitation step ΔU of the field. In the data that we present next, the electrode potential is increased by 0.5 V between each measurement, thus resulting in a detection threshold of $c_{2,E_0} = 174\,\mathrm{mrad\,m^{-1}\,V^{-1}}$ and $c_{3,E_0} = 1.7 \times 10^6\,\mathrm{mrad\,V^{-1}\,m^{-2}}$. Likewise, for a stepwise increase of the coil current by 4 mA, the detection threshold for magnetic deflection measurements is given by $c_{2,B_0} = 21\,\mathrm{mrad\,m^{-1}\,mA^{-1}}$ and $c_{3,B_0} = 2.2 \times 10^5\,\mathrm{mrad\,mA^{-1}\,m^{-2}}$.

V. RESULTS AND DISCUSSION

A. Dipole strength

The electric and magnetic deflection field strengths are independently measured, for both the E–B–E configuration that provides a deflection in the direction of both axes as well as for the B–E–B configuration that deflects the beam in the perpendicular plane. The deflection field strength is measured for both axes separately (distinctively labeled Axis 1 and Axis 2), and we could obtain dipole and quadrupole contributions that exceed the detection limit.

The obtained electrostatic dipole contribution for both axes [Figs. 12(a) and 12(b)] yields $c_{1,E} = 1.95\,\mathrm{mrad/V}$ and the data for both axes overlap within the uncertainty of the measurement. This value is in agreement with the theoretical expectation [Eq. (1)], which yields an expectation of $\tilde{c}_{1,E} = 1.9\,\mathrm{mrad/V}$ for an effective length factor of $k_{t+b} = 1.88$. For the range of data that is shown here, an electrostatic excitation of $U = \pm 20$ V corresponds to a net deflection angle of 40 mrad.

The origin of the seemingly structured noise that is observed in the electric dipole measurement results is most likely caused by the digital to analog converter (DAC). We use a 16 bit DAC that outputs over a voltage span of ± 10 V. This signal is fed to an instrumentation amplifier with a gain of 50, thus leading to a least significant bit resolution of 15 mV. As the electrode potential is increased by 0.5 V in between each measurement, the output steps are confined around $0.5/0.015 = 32 = 2^5$, the fifth bit of the DAC.

The magnetic dipole contributions for both axes do not fully overlap within the uncertainty of the measurement. In addition, the dipole magnitude first increases with approximately 1% of the initial value and afterward reduces back to the initial value. The

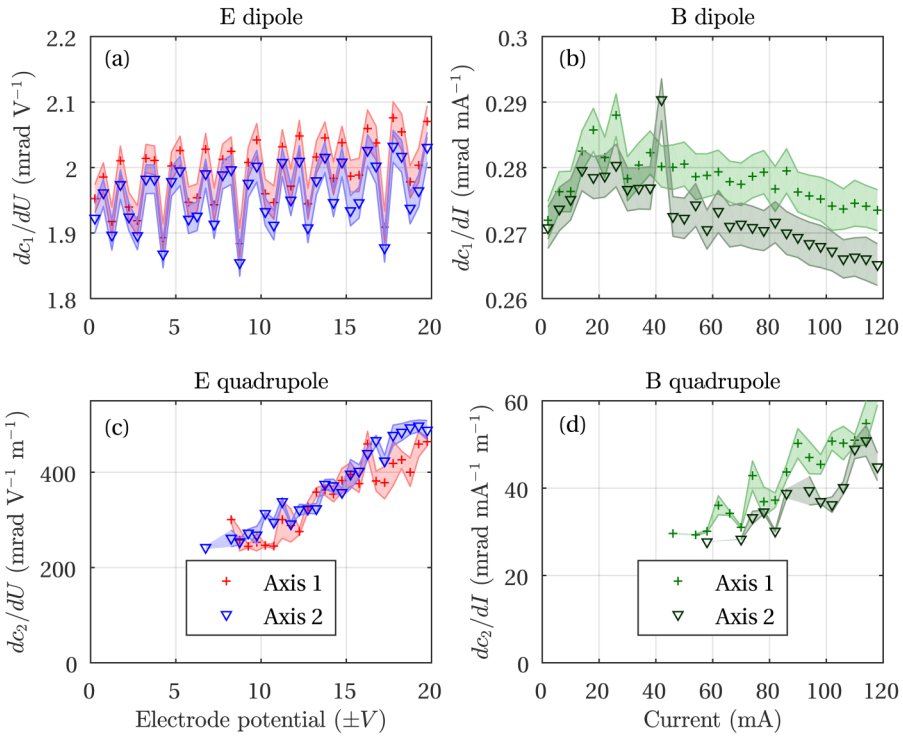

FIG. 12. (a) Electric and (b) magnetic dipole magnitudes, and quadrupole (c) electric and (d) magnetic magnitudes obtained for both axes in the E–B–E configuration. Results obtained at 2 keV beam energy.

average magnetic dipole magnitude reads $c_{1,B} = 0.27$ mrad/mA for Axis 1 and $c_{1,B} = 0.28$ mrad/mA for Axis 2. We make use of the numerically determined $k_m = 1.75$ for deflection in the middle layer in order to estimate the effective value μ of the magnetic material [through Eq. (2) and $B = \mu\mu_0 NI$, with N the number of coil turns and I the current through the coils], and this yields a value of $\mu = 800$ for the magnetic circuit.

B. Multipole strength

The obtained quadrupole contributions display a linear increase as a function of excitation parameter [Figs. 12(c) and 12(d)]. This is a nontrivial result, since the coefficients are supposed to be independent of excitation. However, the former is strictly true only when an increasing excitation would not modify the position of the beam inside the field. This is not the case here, since the dipole fields, that act simultaneously with the distortion field on the beam, move the beam off-axis [Fig. 13(a)].

From the geometry that is shown [Fig. 13(a)], the off-axis effect is most apparent for the characterization of the electric field. Then, the beam propagation through the top layer is responsible for an initial deflection angle of $Uc_{1,E}/2$. This results in an off-axis position for the beam on the third layer that is given by $\delta = U\lambda c_{1,E}/2$.

For a fixed azimuth angle $\phi = \phi_0$, the multipole description [Eq. (8)] can be simplified to

$$U(r, \phi_0) \propto c_1 + 2c_2 r + 3c_3 r^2 + \mathcal{O}(r^3). \quad (13)$$

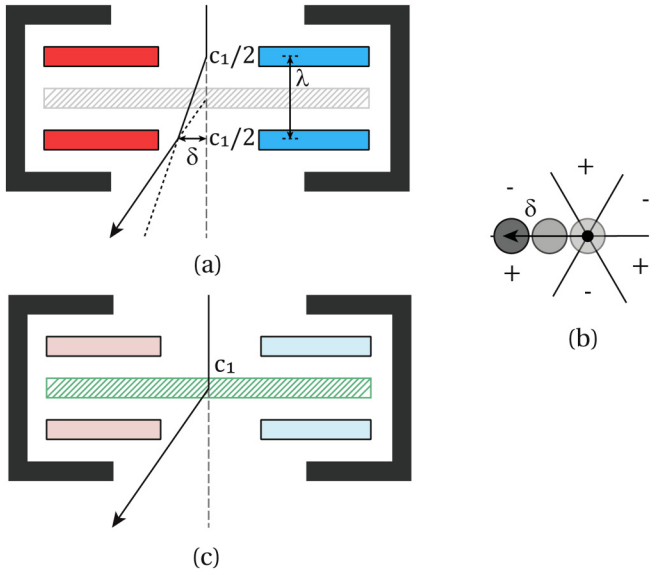

FIG. 13. The effect of a hexapole distortion shows up as a quadrupole contribution that is dependent on the off-axis distance δ. The effect is most pronounced for (a) simultaneous deflection in the top and bottom layers, either electrically or magnetically. (b) A narrow beam that propagates off-axis through a hexapole field initially suffers a quadrupole field, which gradually is taken over by an apparent dipole field. (c) When the deflection is performed by the middle layer only, a definition of δ that is consistent with the former is nontrivial.

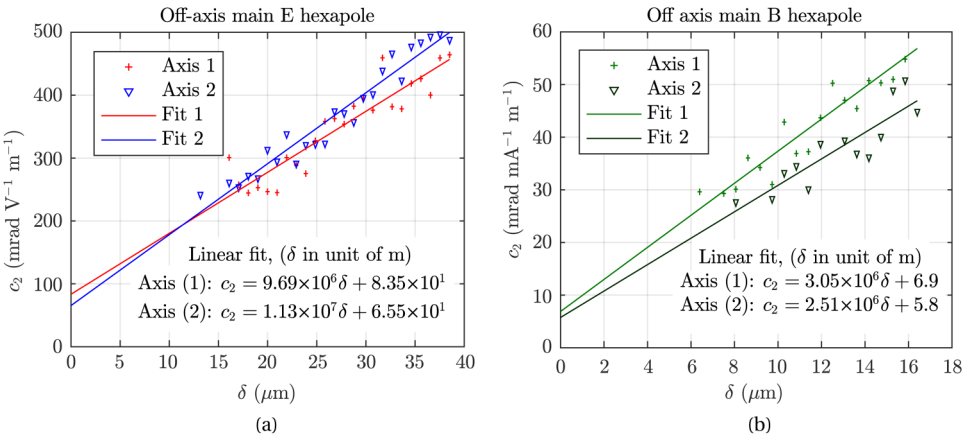

FIG. 14. (a) The obtained electric quadrupole magnitude c_2 as a function of the off-axis position in the bottom layer for both axes and obtained for a 2 keV beam energy. From the slope, the hexapole field strength is approximated, $c_{3,E} = 3.3 \times 10^5$ mrad V^{-1} m^{-2}. (b) The obtained magnetic quadrupole magnitude as a function of the estimated average off-axis position in the middle layer magnetic field. From the slope, $c_{3,B} = 9.27 \times 10^5$ mrad mA^{-1} m^{-2} is obtained.

The field that is generated by an on-axis hexapole can be described by two quadrupole fields that are positioned opposite of one another and rotated with respect to each other by 90° [Fig. 13(b)]. Since a hexapole increases radially quadratic in strength, the incremental change for a fixed azimuthal angle at off-axis position $r = \delta$ is given by

$$\left.\frac{\mathrm{d}U_3}{\mathrm{d}r}\right|_{r=\delta} = 6c_3\delta. \tag{14}$$

This term increases linearly off-axis and we recognize it as the local quadrupole contribution, through $6c_3\delta \equiv 2c_2$. By plotting the obtained c_2 terms as a function of δ [Fig. 14(a)], the hexapole strength is approximated from the slope of the linear curve that fits the data, and we find $c_3 = 3.3 \times 10^5$ mrad V^{-1} m^{-2}. When the offset of the linear fit is interpreted as the residual quadrupole distortion, a value of $c_{2,E} = 7.5 \times 10^1$ mrad V^{-1} m^{-1} is obtained.

A similar analysis that would yield the hexapole magnitude of the central magnetic layer is less trivial, since an expression for the off-axis position δ would be less intuitive [Fig. 13(c)]. For this, we assumed a value of δ that corresponds to the off-axis position of the beam as it is propagated halfway through the field. A linear fit through the data points is obtained with this assumption [Fig. 14(b)], and a hexapole magnitude of $c_{3,B} = 9.27 \times 10^5$ mrad mA^{-1} m^{-2} was found.

The obtained quadrupole coefficients now enable an estimate of wedge angle β_2 inside the various layers of the structure. For the main electric deflection field (top and bottom layers), in accordance with Eq. (10), we find a wedge angle $\beta_{\mathrm{top+bottom}} = 19$ mrad. The wedge angle in the middle layer is determined through the magnetic dipole and quadrupole coefficients and results in $\beta_{\mathrm{middle}} = 7$ mrad.

C. Overview of obtained fields

An overview of the measured and numerically approximated deflection coefficients is given in Table I. The data for deflection in the direction perpendicular to the two axes (B–E–B configuration) are obtained in line with the above outlined methods as well. The integration of the EBE separator in a setup in which the crossover plane of the beam coincides with the device, such as in Fig. 1(a), results in feasible excitation values for low-keV beam energies. In contrast, for applications where the beam is spread out, the application is currently limited by the astigmatism caused by c_2, which at a working distance of 25 mm and for a beam waist of 10 μm results in conservative numbers $d_2^{\mathrm{spot}} \sim 500$ nm and $d_3^{\mathrm{spot}} \sim 150$ nm in accordance with Eq. (8). We expect that improved machining accuracy for the wedge angles may improve the off-axis performance of the device for the latter application.

Finally, we observe that the electric dipole contribution from the top and bottom excitations is larger than that of the middle layer, while the opposite behavior is observed for the magnetic dipole contributions. This observation is ascribed to the difference in gap width, which is 500 μm for the outer layers and 300 μm for the middle layer in the device that we tested. Hence, the magnetic resistance in the middle layer is smaller than that of the outside layers and this leads to an increase in magnetic deflection per mA excitation, since an equal number of coil windings and thus magnetic flux is used in the central layer and for the outer layers combined. Contrarily, the electric dipole coefficients for the outer layers are larger than the central layer despite the higher field strength in the central layer at equal excitation. This is explained by the double passage of a deflection field in the outer layers (refer Fig. 4) and thus an effective increase in deflector area.

TABLE I. Overview of the obtained electric and magnetic field multipole strengths, depending on the level of field excitation and at 2 keV beam energy. Q represents the excitation method ($Q \equiv$ mA for magnetic excitation and $Q \equiv$ V for electric excitation). Entries are blank when no sufficient data points for sampling are obtained.

	Electrostatic ($Q \equiv$ V)		Magnetic ($Q \equiv$ mA)	
	Top and bottom	Middle layer	Top and bottom	Middle layer
c_1/Q (mrad Q^{-1})	1.98	1.22	1.68×10^{-1}	2.75×10^{-1}
c_2/Q (mrad m^{-1} Q^{-1})	7.5×10^1	…	…	6.35
c_3/Q (mrad m^{-2} Q^{-1})	3.50×10^6	…	…	9.27×10^5

VI. CONCLUSIONS

We have built a versatile miniature electron optical device (Fig. 9) that is demonstrated for use as an electron beam separator and that can principally also be deployed as an energy analyzer and monochromator. The incorporation of two parallel axes in the device allow for integration with multi-axis MEMS based electron optical setups. The device departs from conventional beam separator designs by spatially separating the electric and magnetic fields in different layers. In this way, three deflection dipole layers are realized that can accommodate either an electric or magnetic field.

The obtained magnitudes for deflection of the beam in the direction of the other axis are obtained as an electric dipole, $c_{1,E} = 1.98\,\mathrm{mrad/V}$, and a magnetic dipole with a strength given by $c_{1,B} = 0.275\,\mathrm{mrad/mA}$. The method that we used was not sensitive enough for direct measurement of the hexapole distortion coefficient, but these coefficients were obtained from the slope in the quadrupole data points.

ACKNOWLEDGMENTS

The EBE separator concept was developed by P. Kruit, M. A. R. Krielaart, and D. J. Maas. Image registration and processing were done by S. V. Loginov and M. A. R. Krielaart. The authors acknowledge technical support for the mechanical design by Ruud van Tol and Youp van Goozen, flexible PCB design by Han van der Linden, and electrical supplies design by Paul Keijzer. M. A. R. Krielaart also acknowledges experimental support from J. te West during initial evaluation experiments. We acknowledge financial support for this work by the Dutch Research Council (NWO) and the Gordon and Betty Moore Foundation. D. J. Maas gratefully acknowledges support by Hitachi High Technologies for his contribution to this work.

DATA AVAILABILITY

The data that support the findings of this study are available from the corresponding author upon reasonable request.

REFERENCES

[1]H. Müller, D. Preikszas, and H. Rose, "A beam separator with small aberrations," J. Electron Microsc. **48**, 191–204 (1999).
[2]P. W. Hawkes, "Aberration correction past and present," Philos. Trans. R. Soc. A **367**, 3637–3664 (2009).
[3]E. Plies, K. Marianowski, and T. Ohnweiler, "The Wien filter: History, fundamentals and modern applications," Nucl. Instrum. Methods Phys. Res. Sect. A **645**, 7–11 (2011).
[4]N. Sillon and R. Baptist, "Micromachined mass spectrometer," Sensor Actuat. B **83**, 129–137 (2002).
[5]M. Nicklaus and F. Hasselbach, "Wien filter: A wave-packet-shifting device for restoring longitudinal coherence in charged-matter-wave interferometers," Phys. Rev. A **48**, 152–160 (1993).
[6]H. W. Mook and P. Kruit, "Optics and design of the fringe field monochromator for a Schottky field emission gun," Nucl. Instrum. Methods Phys. Res. Sect. A **427**, 109–120 (1999).
[7]H. W. Mook and P. Kruit, "Construction and characterization of the fringe field monochromator for a field emission gun," Ultramicroscopy **81**, 129–139 (2000).
[8]H. Dohi and P. Kruit, "Design for an aberration corrected scanning electron microscope using miniature electron mirrors," Ultramicroscopy **189**, 1–23 (2018).
[9]R. M. Tromp, J. B. Hannon, A. W. Ellis, W. Wan, A. Berghaus, and O. Schaff, "A new aberration-corrected, energy-filtered LEEM/PEEM instrument. I. Principles and design," Ultramicroscopy **110**, 852–861 (2010).
[10]E. Bauer, "LEEM and UHV-PEEM: A retrospective," Ultramicroscopy **119**, 18–23 (2012).
[11]R. M. Tromp, J. B. Hannon, W. Wan, A. Berghaus, and O. Schaff, "A new aberration-corrected, energy-filtered LEEM/PEEM instrument II. Operation and results," Ultramicroscopy **127**, 25–39 (2013).
[12]A. B. Bok, J. B. le Poole, J. Roos, and H. de Lang, "Mirror electron microscopy," in *Advances in Imaging and Electron Physics* (Elsevier, 2017), pp. 99–192.
[13]M. A. R. Krielaart and P. Kruit, "Potentially programmable virtual phase plate for electron beams," Microsc. Microanal. **25**, 92–93 (2019).
[14]P. Kruit, "The role of MEMS in maskless lithography," Microelectron. Eng. **84**, 1027–1032 (2007).
[15]J. Harrison, O. Paydar, Y. Hwang, J. Wu, E. Threlkeld, P. Musumeci, and R. N. Candler, "Fabrication process for thick-film micromachined multi-pole electromagnets," J. Microelectromech. Syst. **23**, 505–507 (2014).
[16]J. Harrison, Y. Hwang, O. Paydar, J. Wu, E. Threlkeld, J. Rosenzweig, P. Musumeci, and R. Candler, "High-gradient microelectromechanical system quadrupole electromagnets for particle beam focusing and steering," Phys. Rev. Spec. Top. Accel. Beams **18**, 023501 (2015).
[17]P. Kruit, "Introduction to charged particle optics," Delft University of Technology, lecture notes (2015) (available on request).
[18]S. Tumanski, *Handbook of Magnetic Measurements* (Taylor & Francis Ltd., 2016).
[19]H. Bay, A. Ess, T. Tuytelaars, and L. V. Gool, "Speeded-up robust features (SURF)," Comput. Vis. Image Underst. **110**, 346–359 (2008).
[20]MATLAB, "Detect SURF features and return SURFPoints object," https://nl.mathworks.com/help/vision/ref/detectsurffeatures.html (last accessed August 2019).